Influence of OH^- on the initiation and growth mechanism of pore structure during microarc oxidation of Ti-6Al-4 V alloy

Zongqing Liu [a], Wei Shi [a b], Song Xiang [a], Fei Liu [a b], Upadrasta Ramamurty [b c]

[a]

Guizhou Key Laboratory of Materials Mechanical Behavior and Microstructure, College of Materials and Metallurgy, Guizhou University, Guiyang 550025, PR China

[b]

School of Mechanical and Aerospace Engineering, Nanyang Technological University, Singapore, Singapore

[c]

Institute of Materials Research and Engineering (IMRE), Agency for Science, Technology and Research (A*STAR), 2 Fusionopolis Way, Innovis #08-03, Singapore 138634, Republic of Singapore

Abstract

The presence of pores in a microarc oxidation (MAO) coating is an inherent characteristic that results from the expulsion and rapid solidification of molten material during the MAO process. The pore size in the MAO coating on the titanium alloy strongly affects the biocompatibility, but how to control it is unclear. The present study utilizes the advantages of NaOH to modulate pore size and plasma discharge, thereby effectively regulating the pore structure of the coating. The FIB-lift-out method was employed to directly extract the cross-sectional samples from the coating, enabling a detailed investigation of the pore microstructure using transmission electron microscopy (TEM). The structure surrounding the discharge channels exhibit layered zoning characteristics, with an amorphous layer near the discharge channel and a distinct crystal structure further away from it. The addition of NaOH enables the regulation of electrochemical and energy release processes, while also facilitating efficient discharge and spark generation to effectively disrupt the oxide layer and establish a plasma discharge channel.

Graphical abstract

The presence of pores in a microarc oxidation (MAO) coating is an inherent characteristic resulting from the expulsion and rapid solidification of molten material during the MAO process. The pore size of the MAO coating on the titanium alloy strongly affects the biocompatibility, but how to control this effect is unclear. The present study utilizes the advantages of NaOH to modulate pore size and plasma discharge, thereby effectively regulating the pore structure of the coating. The FIB-lift-out method was specifically employed to directly extract cross-section samples from the surface of the microarc oxidation coating, enabling a detailed investigation of the pore microstructure using transmission electron microscopy (TEM). The structure surrounding the discharge channel exhibits layered zoning characteristics, with an amorphous main structure near the discharge channel and a distinct crystal structure further away from it. The addition of NaOH ultimately enables the regulation of electrochemical and energy release processes while also facilitating efficient discharge and spark generation to effectively disrupt the oxide layer and establish a plasma discharge channel.

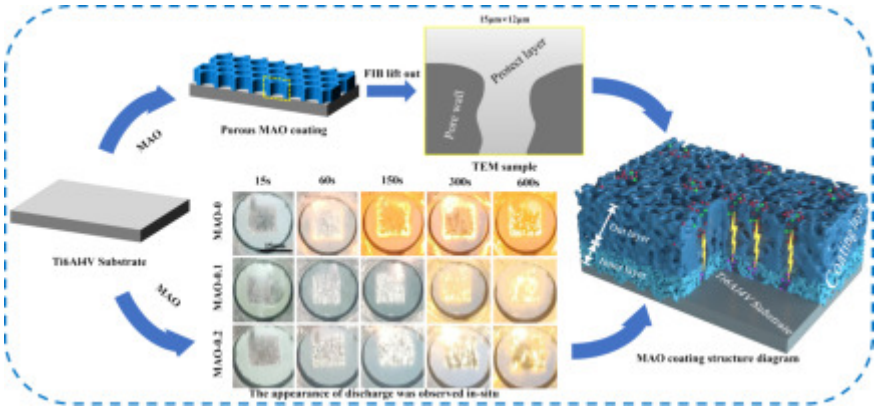

Keywords
Titanium alloy
Microarc oxidation
Pore size
NaOH concentration
Pore microstructure

1. Introduction

Titanium and its alloys are extensively used as biomedical implants due to their excellent biocompatibility and mechanical properties [1,2]. To enhance the wear resistance of such implants, ceramic coatings fabricated using techniques such as microarc oxidation (MAO), thermal spraying, and laser cladding have been explored [[3], [4], [5], [6]]. MAO can result in a porous coating while maintaining excellent biocompatibility [7,8], which is sensitive to the pore size and density [9,10]. The micro- and nano-scale pores created during MAO [11,12] reduce the elastic modulus of the coating compared to that of the base metal and enhance its ability to mechanically interlock with the natural bone [13,14]. The porous structure also enables efficient material transfer between the implant and human bones [[15], [16], [17]]. Additionally, the behavior of cells on the surface of implanted materials is intricately linked to the structural characteristics of the material surface. Prior research has shown that the specific characteristics of pores influence cell morphology, differentiation, and secretion of the extracellular matrix [[18], [19], [20]]. When the coating possesses nanoscale pores, it can enhance cellular adhesion [11], protein adsorption and stimulate osteoblast migration. When its size is in micron-scale, it can facilitate cell diffusion and proliferation [12]. Li et al.'s study showed that a pore size of about 10 μm can enhance bone-induced protein adsorption, ion exchange, and osteoid apatite formation, in addition to the promotion of the adhesion, proliferation, and differentiation of osteoblasts [21]. Therefore, in order to obtain an MAO coating with a predetermined pore structure, a detailed understanding of the mechanism of pore formation is essential.

Keeping the above in view, several studies have focused on the pore structure optimization in MAO coatings on Ti and its alloys through the tuning of the process parameters and electrolyte composition. Zhou et al. [22] and Kuroda et al. [23] demonstrated that an increase in the processing time or voltage, respectively, can lead to an increase in the pore diameter, while reducing the number of pores per unit area. Li et al. [24], who added K_2ZrF_6 to a silicate electrolyte, reported that with an increase in the concentration of K_2ZrF_6, an initial decrease and a subsequent increase in both the number and diameter of micropores on the surface of the MAO coating. Recently, Guo et al. [25] fabricated ultralow porosity coatings by incorporating graphene oxide into a silicate electrolyte using a one-step PEO

method on the surface of the Ti-6Al-4 V alloy. The investigation revealed that the addition of graphene oxide to the one-step PEO process significantly mitigates the surface as well as overall porosity, while simultaneously promoting the pore shape.

According to prior studies, controlling the morphology of submicron-scale pores or grooves in the MAO process remains a challenge, despite attempts to modify the applied voltage or oxidation time [[26], [27], [28]]. The electrochemical process during the MAO treatment can be regulated by adjusting the concentration of NaOH in the electrolyte, as indicated in several studies [29,30]. Furthermore, the formation of pores is influenced by the NaOH concentration. Rehman et al. [30] revealed that increasing the concentration of NaOH in the electrolyte led to a reduction in the arc voltage during the MAO process and resulted in the formation of a thicker coating. They report that an increase in the NaOH concentration to 2 g/L significantly reduced the porosity, number of defects, and width of the discharge traces. Zhou et al. [31] investigated the impact of the NaOH concentration on the macroporous microstructure by adjusting the NaOH concentration in the electrolyte for a secondary oxidation treatment. Their results reveal that the addition of 20 g/L NaOH to the electrolyte facilitated the formation of relatively fine macrospores on the surface of the samples.

NaOH is commonly added as an additive to silicate electrolytes, where SiO_3^{2-} aids in forming the SiO_2 films. Traditionally, NaOH has been used as a pH regulator. However, its specific role in the film formation process remains unclear. Consequently, the focused ion beam (FIB) lift-out method is utilized in the present study for direct observation of micropore nanostructures. Real-time in situ monitoring of discharge sparks during the MAO process was achieved using an underwater optical periscope. The integration of these techniques facilitated a deeper understanding of pore formation mechanisms and elucidation of the impact of additives on MAO coating formation, thereby enabling precise regulation of electrolyte composition. In this study, a comprehensive investigation was conducted to explore the influence of varying concentrations of NaOH incorporated into the silicate electrolyte solution on both the morphological and compositional changes observed in the Ti6Al4V alloy coating. By combining these coating designs and research strategies with the electrical characteristics of coating growth, we investigated the influence mechanism of NaOH concentration on the MAO process and established a growth mechanism model for oxides in MAO coatings.

2. Materials and methods

The Ti6Al4V alloy plate was sectioned to obtain disc-shaped samples measuring 15 mm × 15 mm × 3 mm. The composition of the alloy (wt%) was Al 5.5–6.8, V 3.5–5.5, C < 0.10, *N* < 0.05, H < 0.015, O < 0.20 and Fe < 0.30; the remainder was Ti. When the Ti6Al4V alloy sample serves as the anode, a stainless steel electrolyser functions as the cathode. The base material was polished using a step-by-step process with waterproof silicon carbide (SiC) sandpapers (#200, #400, #600, and #1000). It was then subjected to ultrasonic cleaning with ethanol and distilled water in sequence before being air-dried.

The electrolyte composition and pH are shown in Table 1; a pH meter (PHS-3C, Lida, China) was used for the pH measurements. The frequency and duty cycle are set at 600 Hz and 10 %, respectively, for the applied waveform. The MAO coatings are denoted as MAO-0, MAO-0.05, MAO-0.1, MAO-0.15, and MAO-0.2 based on the NaOH concentration in the electrolyte. A constant current of 0.16 A cm^{-2} was maintained across all samples throughout the entire 10-min processing duration. During MAO, the alloy sample was fully immersed in a 5 L electrolyte solution. The discharge sparks of the sample were observed in situ, using an underwater optical periscope and captured with a camera, as schematically illustrated in Fig. 1. Subsequently, the sample was rinsed with distilled water to prevent any additional

deposition of electrolyte components during the drying stage.

Table 1. Sample designation and the NaOH concentration in the electrolyte and the corresponding pH values of the solution.

Sample designation	Base electrolyte (M/L)	Additive (M/L)		pH
MAO-0		–	–	12.50
MAO-0.05		0.05	NaOH	12.54
MAO-0.1	0.15 Na_2SiO_3 + 0.02 $C_3H_8O_3$	0.10	NaOH	12.58
MAO-0.15		0.15	NaOH	12.60
MAO-0.2		0.20	NaOH	12.98

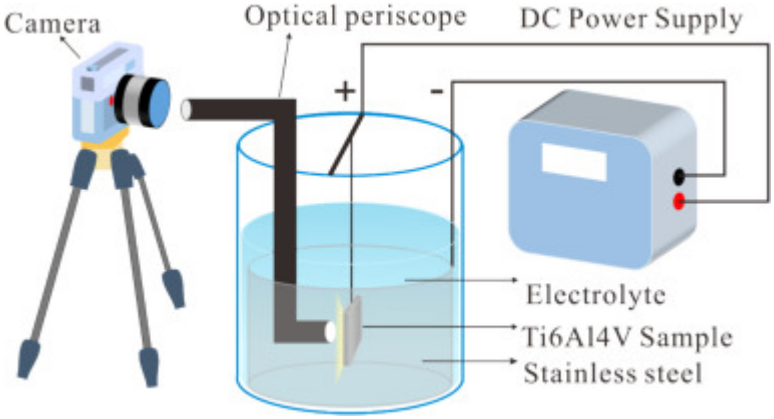

1. Download: Download high-res image (158KB)
2. Download: Download full-size image

Fig. 1. A schematic diagram of the experimental set up utilized for observing the discharge sparks in situ using an underwater optical periscope during the MAO process.

The surfaces and cross-sections of the coatings were examined using a field emission scanning electron microscope (TESCAN MIRA LMS, Czech Republic). A layer of gold film was deposited onto the surface of the sample before microscopy. An acceleration voltage of 3 kV was utilized for topographic examination, while 15 kV using for energy spectrum mapping. The microscope was equipped with a SE2 secondary electronic detector. The coating thickness was determined by selecting 20 different cross-sectional locations (imaged at 1500×) for each sample and conducting random tests to obtain the average thickness.

The commercially-available software Image-Pro Plus 6.0 was used to calculate the surface porosity and pore sizes in all the coatings, using the SEM micrographs. The surface porosity was calculated as follows: surface porosity = (micropore area/total area) × 100 %.

The phase compositions of the coating sample surfaces were analysed using an X-ray diffractometer (XRD, Rigaku SmartLab SE, Japan). CuKα1 radiation with a wavelength of 1.54056 Å and an operating voltage of 40 kV was used for scanning in the range of 20°-80° at a scanning speed of 2°/min. The Raman scattering spectra were acquired using a Horiba Scientific-LabRAM HR Evolution Raman spectrometer, which was equipped with an excitation wavelength of 514 nm.

The microstructure of the coatings was investigated using transmission electron microscopy (TEM, JEOL 2100F, 200 kV). Cross-sectional samples for TEM analysis were prepared via focused ion beam (FIB, Crossbeam 550, ZEISS) milling. To protect the coating surface from any FIB damage, two

platinum (Pt) layers, including a thin Pt layer with thickness of 50 nm deposited under electron beam (2 kV, 5 nA) and an overlapping Pt layer with thickness of 1 μm deposited under FIB using Ga^+ source, were deposited onto the coating surface. Next, a series of procedures including bulk-out (30 kV, 15 nA), medium thinning (30 kV, 3 nA), U-cut (30 kV, 3 nA), lift-out, transfer, and fine thinning (30 kV, 100 pA) were used to prepare TEM samples. To avoid any further FIB damage, the top and bottom surfaces of all TEM samples were cleaned at a low voltage and beam current (5 kV, 10 pA). Selected area electron diffraction patterns (SAED) and high-resolution TEM (HRTEM) images were captured, while EDS attached to the TEM instrument was used for the elemental analysis.

3. Results

3.1. Voltage response of the MAO treatment

The voltage–time response curves during the MAO process with varying NaOH concentrations are shown in Fig. 2. Within the treatment time of 10 min, the diagram can be divided into three distinct regions: conventional anodic, spark discharge, and microarc oxidations [[32], [33], [34]]. The voltage-time curves clearly demonstrate a downwards shift as the concentration of NaOH in the electrolyte increases from 0 to 0.2 M/L. This decrease can be attributed to the enhanced electrolyte conductivity, resulting from the higher NaOH concentration, leading to a decrease in the partial voltage applied across the electrolyte [35]. During the anodizing stage, there was almost no difference between the MAO coatings obtained in all electrolytes with different NaOH concentrations, and the voltage increased linearly. After the addition of NaOH, the breakdown voltage [36] of the coating gradually decreases due to an enhanced electron avalanche process, exhibiting a significant reduction compared to that observed without NaOH (Table 2). It is worth noting here that Han et al. [37] also found that when KOH was added to the electrolyte, the breakdown voltage decreased. After entering the spark discharge stage, a discontinuous microarc oxide film starts to form on the sample surface. However, its growth rate remains minimal. As the voltage increases, the microarc oxidation stage gets initiated; as it is closely linked with the spark discharge, making it difficult to distinguish between them. Throughout the reaction process, the voltage in the electrolyte without any NaOH remained consistently greater than that in the electrolyte containing NaOH, suggesting a lower energy consumption in the latter, as the voltage variation is closely correlated with the energy consumption (Q), which can be calculated using the equation: $Q = Ia\int tbtaUtdt$ for the MAO process [38], where I_a represents the average current, t_b denotes the time required to reach breakdown voltage, t_a is the end time of the MAO reaction, and U_t is the change in voltage over time. Table 2 compares the Q values for different NaOH concentrations during the reaction process. Among them, MAO-0.2 (−359.8 $J{\cdot}mm^{-2}$) exhibited the lowest Q, which was 15 % lower than that of MAO-0. Therefore, the addition of NaOH not only decreases the breakdown voltage of the coating sample, which leads to easy spark discharge, but also reduces the Q needed.

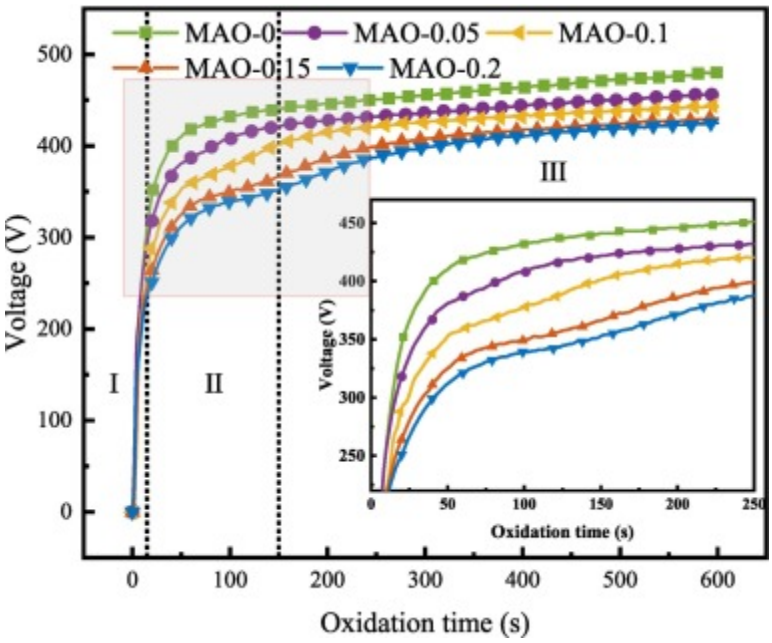

1. Download: Download high-res image (339KB)
2. Download: Download full-size image

Fig. 2. Voltage-time response at 0.16 A cm^{-2} in the electrolyte with different NaOH concentrations.

Table 2. Energy consumption and breakdown voltage of coatings with different concentrations of NaOH.

Sample tag	Breakdown Voltage (V)	Energy consumption (J·mm^{-2})
MAO-0	294	423.218
MAO-0.05	273	403.592
MAO-0.1	247	388.158
MAO-0.15	241	368.482
MAO-0.2	231	359.769

The appearance of discharge at different stages of MAO is shown in Fig. 3. Based on the voltage-time responses presented in Fig. 2, three representative samples, namely, MAO-0, MAO-0.1, and MAO-0.2, were selected for observing the discharge characteristics. After immersing the samples in the electrolyte and applying the voltage for 15 s, a thin anodic oxide layer forms on the surfaces of all the samples, accompanied by numerous small uniform white bubbles. Upon entering the spark discharge stage, multiple small and low-intensity sparking points emerge on the sample surfaces. The size and brightness of the sparks gradually increase, while their point density also increases with the applied voltage, up to 60 s. It is worth noting that there are differences in the discharge characteristics of the samples supplemented with NaOH and those without NaOH. Specifically, at the edge of the MAO-0 sample, a more intense orange–yellow colour was observed. This is confirmed by the high-voltage distribution curve shown in Fig. 2. Furthermore, due to the lower electrical conductivity of the electrolyte used for MAO-0, the surface conductivity of the sample becomes less uniform and exhibits greater edge polarizability than that with the addition of NaOH. Therefore, there is an increased likelihood of charge accumulation at the sample edge, leading to preferential discharge in this region.

At 300 s, the MAO-0.1 and MAO-0.2 samples exhibited distinct microarc discharge characteristics, including larger arc spots and higher densities, accompanied by loud sound bursts and significantly increased oxygen release. During the MAO process, an increase in the size of the discharge and the decrease in the spatial density are related to the number of discharge sites through which the higher anode current is able to pass [39]. Therefore, the addition of NaOH not only promotes uniform discharge on the sample surface, but also reduces the energy consumed throughout the MAO process.

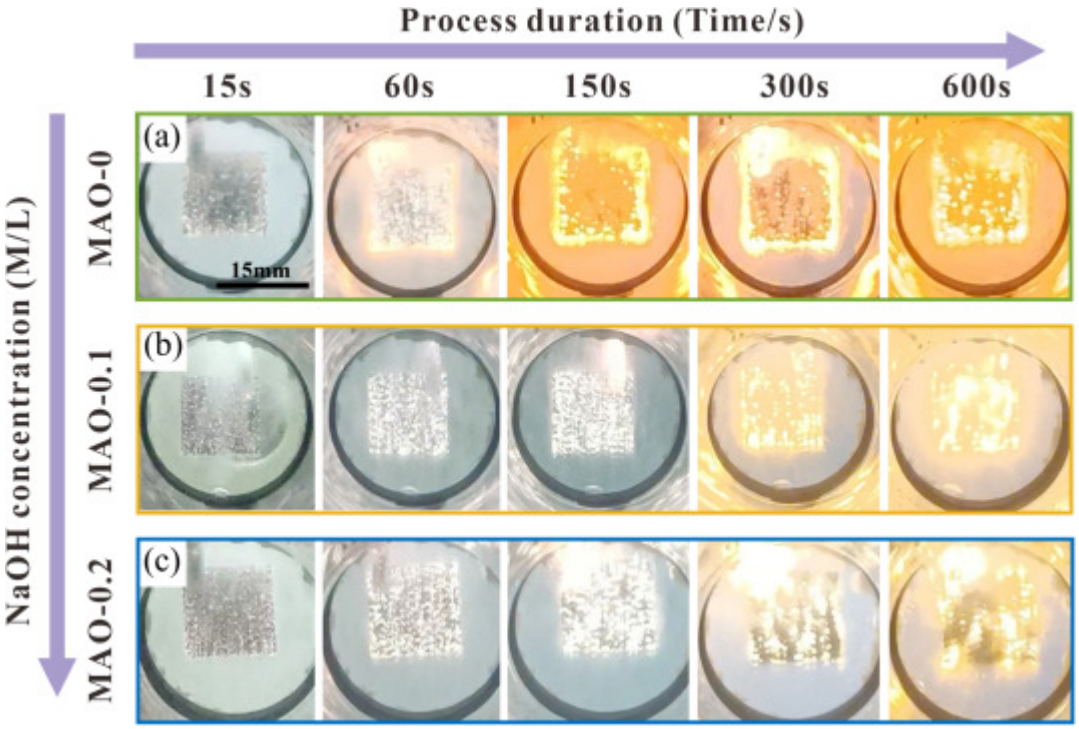

1. Download: Download high-res image (686KB)
2. Download: Download full-size image

Fig. 3. Discharge appearance at various stages of the MAO process: (a) MAO-0; (b) MAO-0.1; (c) MAO-0.2.

3.2. Phase characterization of the MAO coating

The phase structure of the MAO coatings in electrolytes with varying concentrations of NaOH was investigated using XRD. The obtained scans are presented in Fig. 4(a). All the coatings primarily consist of Ti, rutile TiO_2, and anatase TiO_2. In terms of peak intensity, the observed weakening of the Ti peaks can be attributed to an increase in coating thickness. The fractions of each phase observed in the diffraction pattern were quantitatively determined and are presented in Fig. 5. It is evident that an incremental trend is observed for both rutile-type TiO_2 and anatase-type TiO_2 within the coating as the concentration of NaOH increases. It should be noted that rutile is a stable phase at high temperatures, and upon reaching a certain temperature, anatase will undergo conversion into rutile [40]. Prior studies have demonstrated that anatase has enhanced biological activity, while rutile has significantly greater hardness, and, hence, improves the wear resistance of the coating [41].

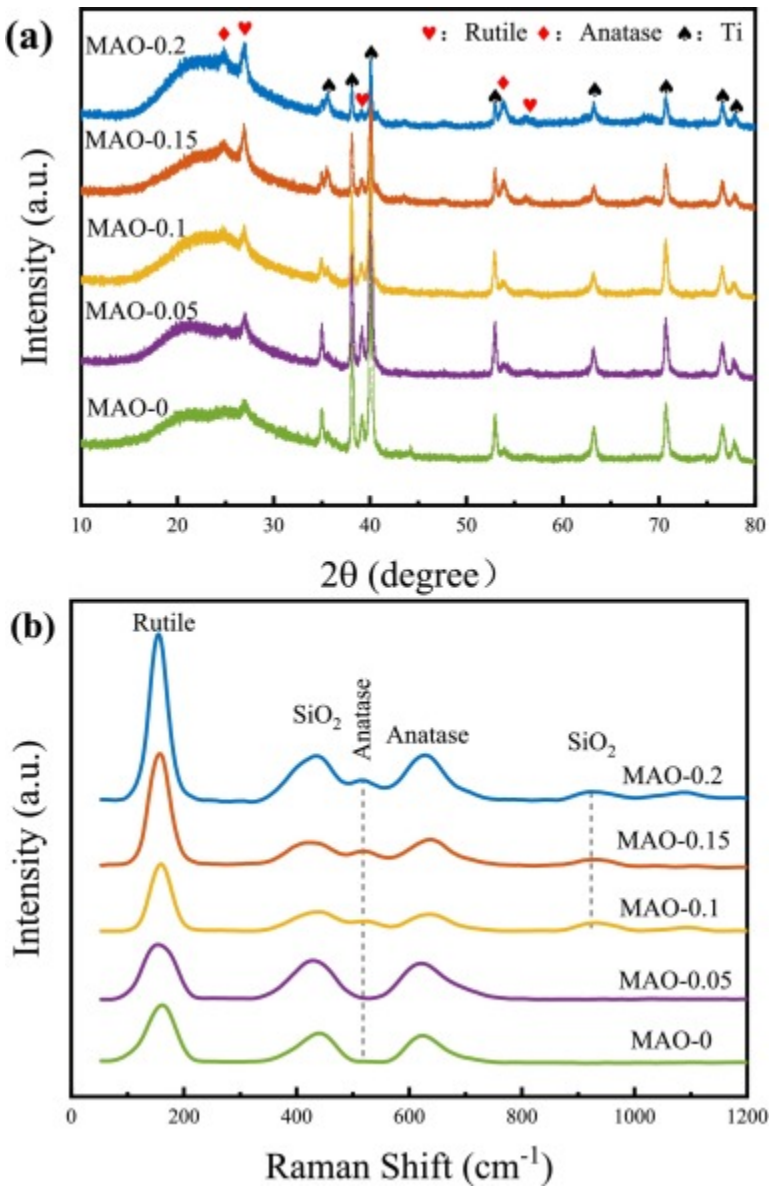

1. Download: Download high-res image (481KB)
2. Download: Download full-size image

Fig. 4. (a) XRD patterns and (b) Raman spectra obtained on different MAO coatings.

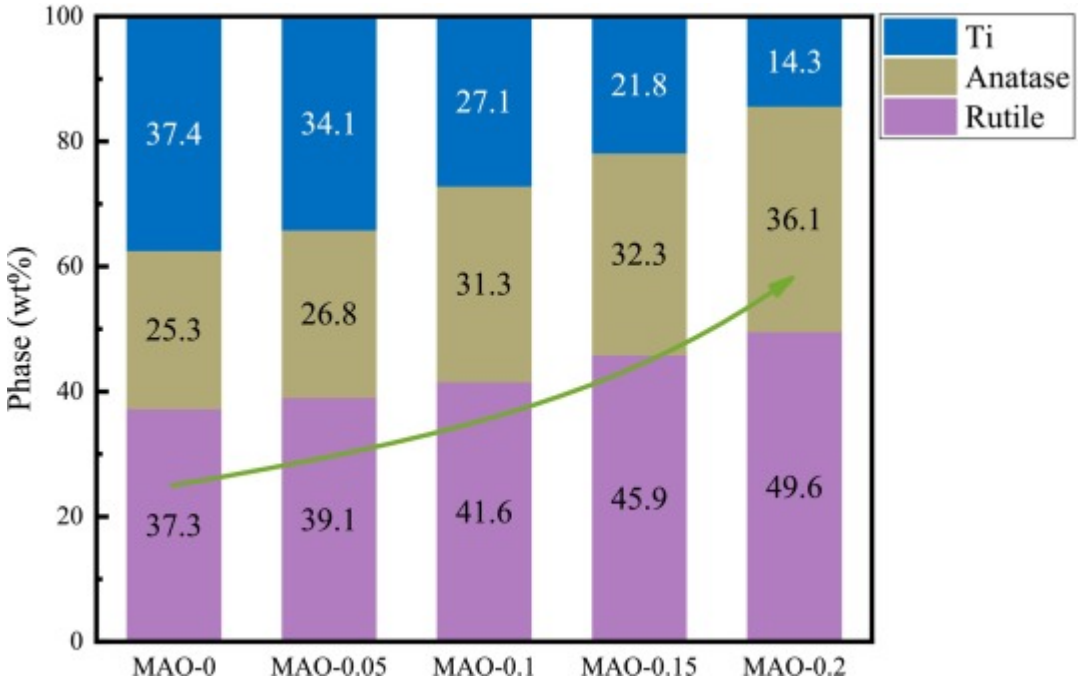

1. Download: Download high-res image (209KB)
2. Download: Download full-size image

Fig. 5. The volume fractions of different phases in the MAO coatings, quantitatively analysed using XRD.

The EDS analysis conducted during the SEM investigation of the MAO coating revealed that Si from the electrolyte was bound to the MAO coating, as shown in Fig. 8. However, no peaks corresponding to any Si-based compounds were detected in the XRD spectra. Since the Si content in the coating exceeds the Ti content, Raman spectroscopy was used to confirm whether there was SiO_2 in its structure. The Raman spectra of the MAO coatings are presented in Fig. 4(b), which reveal the characteristic band positions of TiO_2 and SiO_2 within the MAO coating. The peaks located near 150 cm^{-1} in the Raman spectra are attributed to the presence of rutile TiO_2, while those at approximately 500 and 600 cm^{-1} are attributed to the presence of anatase TiO_2 [42,43]. The peaks observed at approximately 400 and 968 cm^{-1} correspond to SiO_2 [44]. The peaks corresponding to both the rutile TiO_2 and anatase TiO_2 in the coatings increase with the NaOH concentration in the electrolyte, which is consistent with the XRD results.

3.3. Surface morphology of the MAO coating

The surface morphologies of the MAO coatings was examined using SEM; representative images are shown in Fig. 6. An increase in the NaOH concentration is positively correlated with both the quantity and diameter of the micropores in the MAO coating, as shown in Figs. 6((a-1)-(e-1)). The surface porosity and pore sizes in all the coatings, estimated based on the SEM images, are listed in Fig. 7. It indicates that among all the coatings, the MAO-0.15 and MAO-0.2 samples exhibit the highest levels of surface porosity, at 5.2 % and 6.8 %, respectively. The surface porosity of MAO-0.2 is greater than that of all the other coated samples as the size of the discharge channel increases. However, the surface porosities of MAO-0.05 and MAO-0.1 decreased to approximately 2.7 %. In contrast, compared to these two samples (MAO-0.05 and MAO-0.1), the surface porosity of the MAO-0 sample slightly increased due to the formation of a large amount of less dense granular oxides. The micropore diameter gradually increased with the NaOH concentration. These findings suggest that incorporating varying concentrations of NaOH during the MAO process significantly influences both the pore size

and surface porosity of the resulting oxide coating. An increase in the NaOH concentration leads to an increase in the conductivity of the electrolyte system, facilitating plasma discharge generation and, consequently, results in an increase in the micropore quantity. Simultaneously, an intensified arc discharge accelerates charge transfer and material exchange at the interface between the coating and substrate, contributing to the MAO coating degradation and, ultimately, leads to an aperture enlargement. Furthermore, the MAO coating gradually thickens during the reaction process, leading to a reduction in the microarc discharge density on its surface (Fig. 3). However, the energy of individual discharge events increases. Consequently, as the NaOH concentration increases, the pore size expands, while the number of pores per unit area decreases.

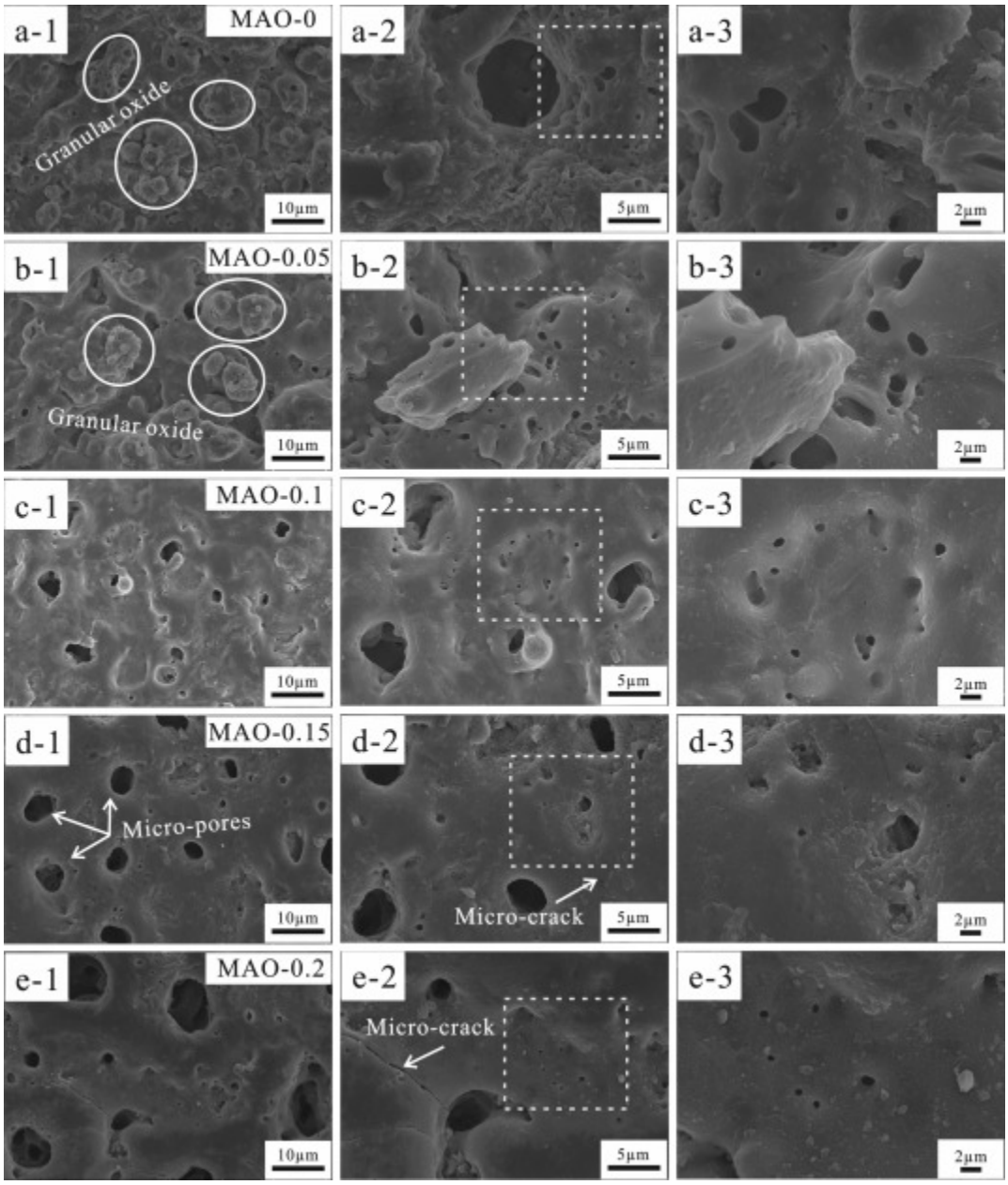

1. Download: Download high-res image (1MB)
2. Download: Download full-size image

Fig. 6. Surface morphologies of the MAO coatings: (a) MAO-0, (b) MAO-0.05, (c) MAO-0.1, (d) MAO-0.15, and (d) MAO-0.2.

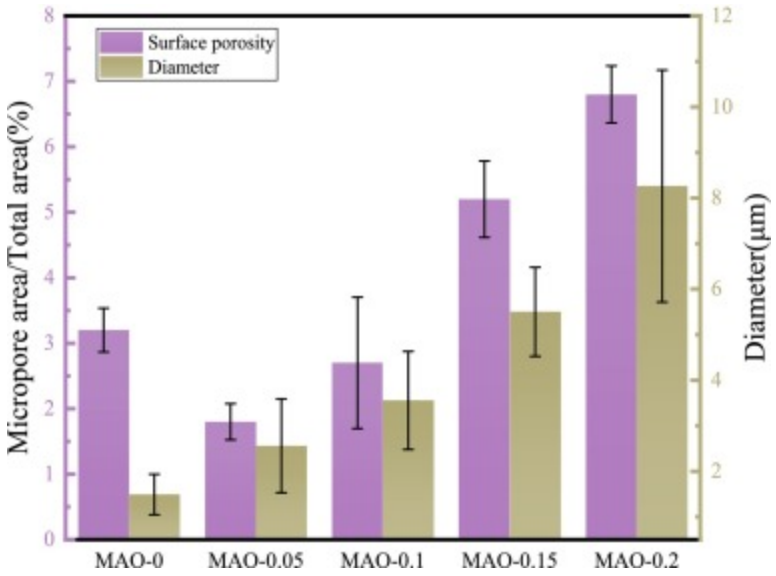

1. Download: Download high-res image (141KB)
2. Download: Download full-size image

Fig. 7. Surface porosity levels and pore sizes in different MAO coatings.

Compared with the sample coated with NaOH, the sample coated without NaOH exhibited pronounced large micropores in specific regions, as evidenced by the higher magnification images shown in Figs. 6((a-2)-(e-2)). It is evident from Fig. 2, Fig. 3 that the addition of NaOH decreases the breakdown voltage of the coating, leading to more uniform discharge. This observation implies that NaOH facilitates discharge while simultaneously reducing the energy required for the coating breakdown. Conversely, in the absence of NaOH, discharging becomes more difficult for the coated sample, resulting in localized high-energy discharges and a limited probability of hole formation. The formation of large micropores results in the generation of a significant quantity of molten oxide due to their higher energy levels. Under high pressure and intense energy, these molten oxides are expelled from the channels, akin to the volcanic eruptions, and subsequently solidify upon coming to contact with the cooler electrolyte. However, due to insufficient time for resolidification, the excess molten oxides fail to adequately cover the original coating surface. In comparison with samples coated with NaOH, tiling the coated surface becomes more feasible because the discharge process exhibits enhanced uniformity and generates fewer molten oxide products. Therefore, the addition of zero or a small amount of NaOH resulted in the formation of numerous granular oxides on the surface of the coated sample, as depicted in Figs. 6(a-1) and (b-1). These granular oxides significantly impact the wear resistance of the coating due to their low density and increased surface roughness. Additionally, the increase in NaOH concentration led to the formation of microcracks on the surface of the MAO-0.15 and MAO-0.2 coatings, significantly compromising their mechanical properties. This phenomenon can be attributed to two factors. First, the addition of NaOH enhances the conductivity of the electrolyte system, thereby promoting MAO reactions and increasing the ejection of molten oxides from discharge channels. Subsequently, during cooling, these molten oxides undergo volume shrinkage-induced internal stress generation. During the breakdown process, the progressive accumulation of internal stresses induces the formation of surface cracks in the coating. Furthermore, due to variations in the thermal expansion coefficients and expansion directions among different phases within the coating, cracking initiates [24].

3.4. Chemical composition of the MAO coating

Results of the elemental compositions of the different MAO coatings, examined using EDS, are shown in Fig. 8. It is clear that all coatings are composed of oxygen (O), aluminum (Al), vanadium (V), titanium (Ti), and silicon (Si). The O content in the coating surpasses 44 %, indicating the predominant presence of oxides containing Ti, Al, and Si. The Si content on the surface of the MAO coating significantly increases due to the insolubility of amorphous SiO_2 in alkaline electrolytes, thereby facilitating its deposition onto the coating surface [45,46]. The presence of Ti, Al, and V in the coating is due to their presence within the matrix of the Ti alloy, while Si originates from an electrolyte containing silicate. Therefore, it can be inferred that the formation of the MAO coating occurs through substrate oxidation and deposition of electrolyte compounds. Teh et al. [47] studied the initial phase of plasma electrolytic oxidation of Ti. Their results showed that a uniformly distributed layer mainly composed of titanium dioxide formed on the substrate surface first, and then, some substances in the electrolyte were observed on the oxide film. Moreover, with an increase in the NaOH content in the Na_2SiO_3 electrolyte, there is a gradual decrease in the mass percentage of Si on the coating surface, while that of Ti gradually increases.

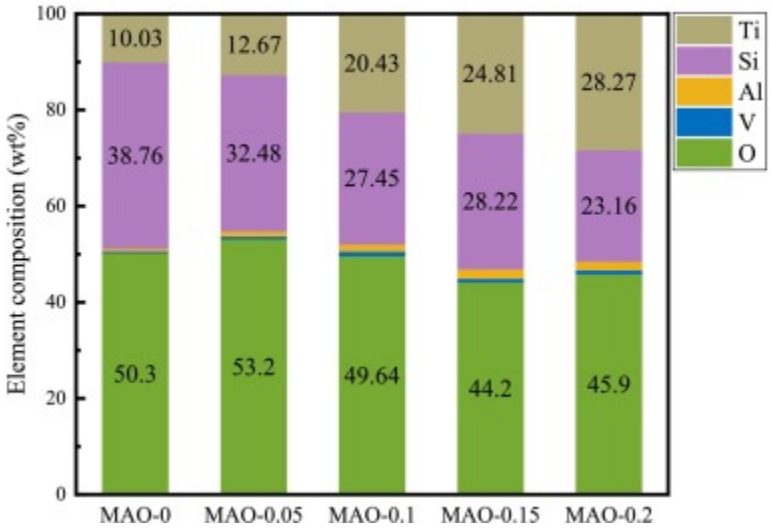

1. Download: Download high-res image (158KB)
2. Download: Download full-size image

Fig. 8. Elemental composition of the different MAO coatings: (a) MAO-0, (b) MAO-0.05, (c) MAO-0.1, (d) MAO-0.15, and (d) MAO-0.2.

Fig. 9 shows the cross-sectional morphologies of the MAO coatings produced with varying NaOH concentrations. On the basis of the observed compositional distributions, the coatings can be partitioned into two layers: an outer layer that is enriched in Si and an inner layer enriched in Ti (as shown in Figs. 9(a-e)). During the MAO process, the thickness of the ceramic coating increases with the NaOH concentration from 17.7 ± 2.7, to 34.9 ± 2.2 μm. The addition of NaOH to the silicate electrolyte system enhances the growth rate of the MAO coating. It can be inferred that a thin anodic oxide layer forms on the Ti6Al4V substrate in the initial stage of the MAO reaction. As the reaction progresses, the weak point in the oxide film is disrupted, resulting in spark discharge. The deposition of the molten oxide leads to the thickening of the oxide coating. The introduction of NaOH into the silicate electrolyte system results in an increase in the OH^- concentration, facilitating the formation of TiO_2 through the arc discharge electrothermic chemical reaction and, consequently, enhances the film thickness [48]. Furthermore, the incorporation of NaOH enhances the electric field intensity and intensifies the reaction kinetics. Due to a strong electric field, anions such as SiO_3^{2-} and OH^- migrate

rapidly towards the surface of the anode. During the subsequent cooling and solidification process, additional molten oxides accumulate on the substrate surface, increasing the film thickness. (See Fig. 10.)

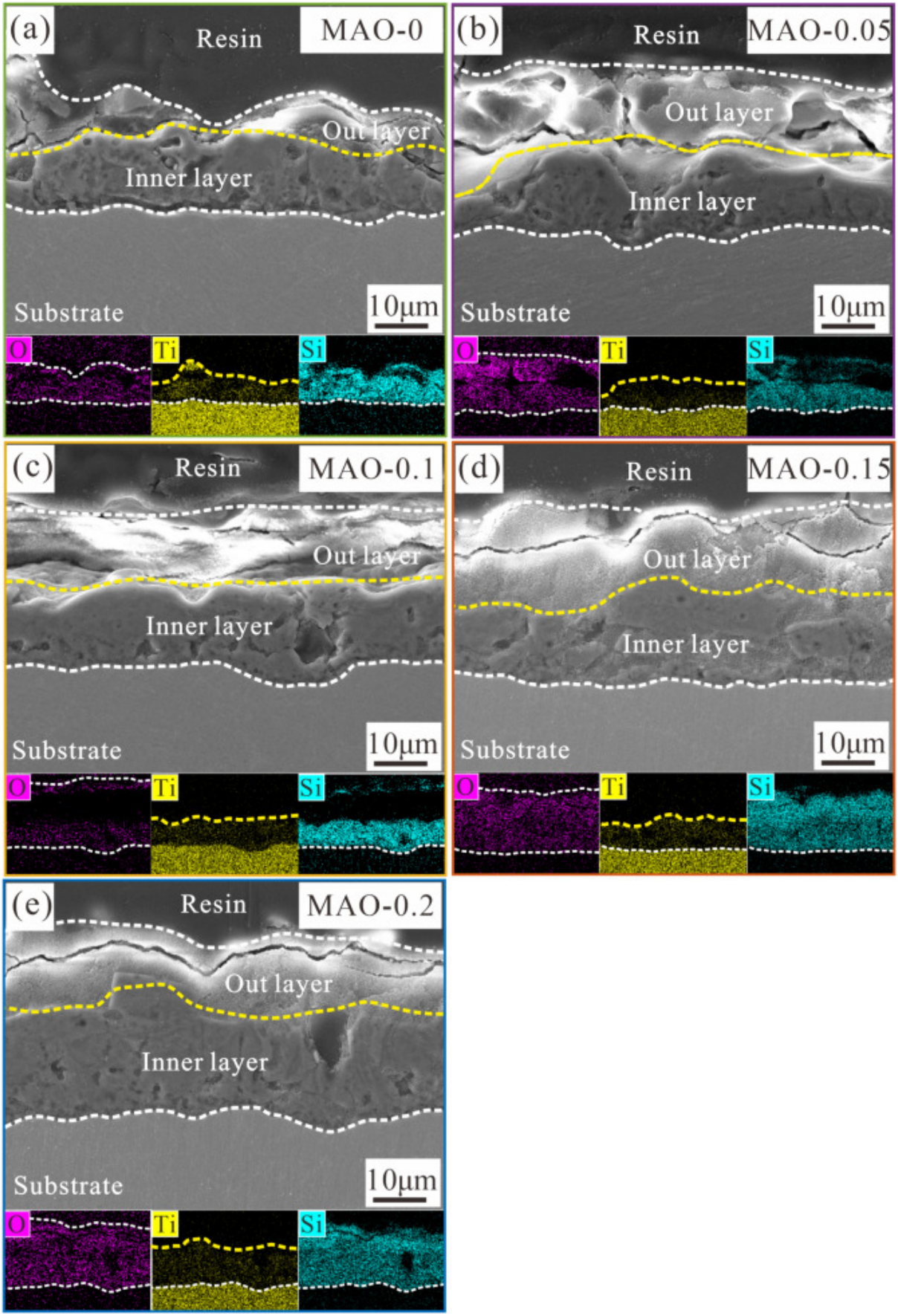

1. Download: Download high-res image (3MB)

2. Download: Download full-size image

Fig. 9. Cross-sectional morphologies and elemental distributions in different MAO coatings: (a) MAO-0, (b) MAO-0.05, (c) MAO-0.1, (d) MAO-0.15, and (d) MAO-0.2.

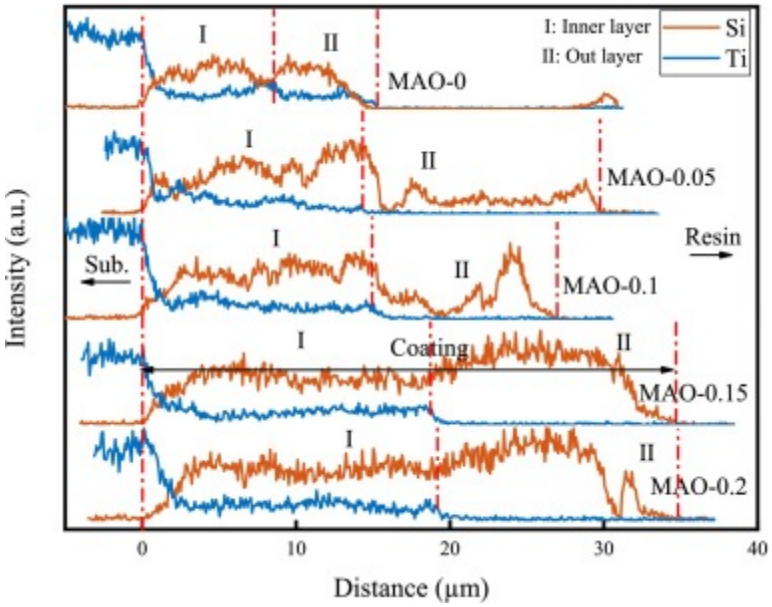

1. Download: Download high-res image (382KB)
2. Download: Download full-size image

Fig. 10. Elemental depth profiles of different MAO coatings.

The elemental distributions across the MAO coatings are shown in Figs. 9(a-e) and 10. It is noteworthy that, compared to the inner layer of the coating, there is a minimal presence of Ti in the outer layer adjacent to the surface, where Si appears to be significantly more concentrated. The primary composition of the outer layer of the coating corresponds to that of a silicate oxide, whereas titanium oxide is mainly distributed in the inner layer. This differentiation becomes more noticeable as the NaOH concentration increases, as shown in Figs. 9(a-e). This observation further supports the notion that the growth of the MAO coating is attributed to matrix oxidation and electrolyte compound deposition.

3.5. TEM analysis of the MAO coatings

The TEM samples were prepared using the FIB lift-out method, which involved direct sectioning of cross-sectional samples from surface holes of the MAO-0.15 sample. To safeguard against any potential damage during the cutting process, Pt was deposited onto the surface. By employing this technique, precise microscopic characteristics of the micropore structure can be obtained, as shown in Figs. 11(a) and (b). A bright field image of region III in Fig. 11(c) is presented in Fig. 11(d), illustrating the presence of hierarchical zoning characteristics surrounding the discharge channel structure. Two representative regions (zones i - ii) were specifically chosen for detailed microstructure analysis. The high-resolution image of region i in Fig. 11 (d), as shown in Fig. 11 (e), reveals a disordered phase, while the presence of a diffraction ring on the outer surface of the discharge channel (Fig. 11(f)) also suggests its amorphous nature. Furthermore, the high-power TEM bright field image (Fig. 11(g)) captured in region ii provides additional evidence for the existence of a noncrystalline layer near the surface of the discharge channel, while a crystalline structure is observed at a distance from it. The high-resolution image displayed in Fig. 11(h) shows a region located far from the discharge channel (region ii). The image reveals a distinguishable ordered phase, although some positions are

intertwined with disordered phases. These findings suggest that the primary phase surrounding the discharge channel is amorphous, while the crystal structure distant from the discharge channel is clearly discernible. The Fourier transforms (FFTs) of microregions A, B, and C in the high-resolution image of region iii (Fig. 11(h)) are depicted in Figs. 11(j), Fig. 11(k), and Fig. 11(l), respectively. Based on the inverse Fourier transforms (IFFTs) corresponding to the microzone locations, region A represents the rutile phase with a crystal face spacing of 3.2 Å, region B corresponds to the anatase phase with a crystal face spacing of 2.4 Å, and region C signifies the silicon oxide phase with a crystal face spacing of 3.4 Å. The calibration results of the selected electron diffraction pattern in Zone iii (Fig. 11(i)) reveal distinct polycrystalline diffraction rings, indicating that the region away from the discharge channel primarily consists of the rutile and anatase phases of TiO_2, with a minor presence of SiO_2 likely dispersed among the nanocrystalline and amorphous forms of TiO_2 grains.

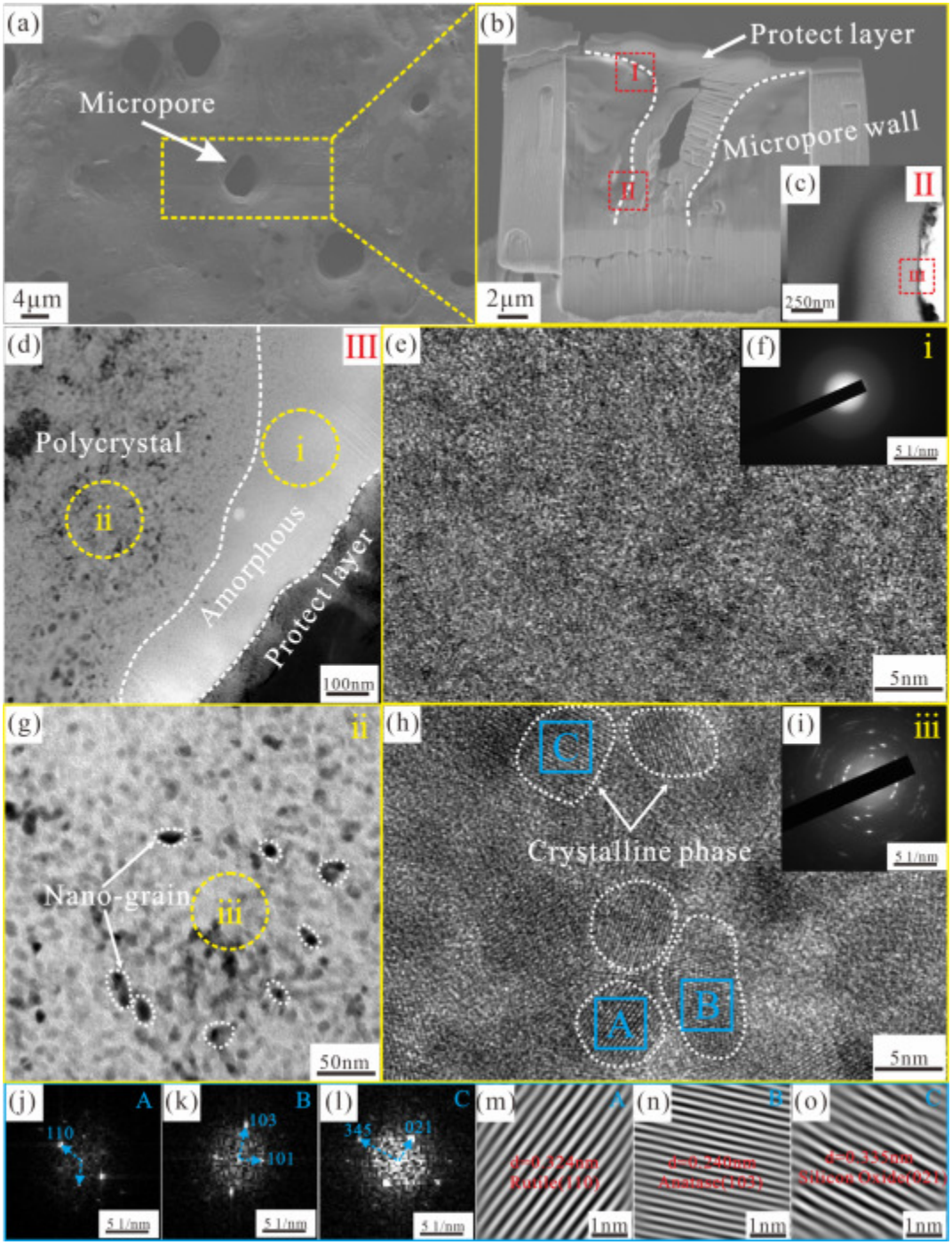

1. Download: Download high-res image (2MB)
2. Download: Download full-size image

Fig. 11. Characterization of the MAO-0.15 sample's coating: (a) A SEM image showing the coating surface; (b) A SEM image illustrating the cross-section of a micropore; (c) a TEM bright field image of area II in Fig. 11(b); (d) a TEM bright field image of the region III in Fig. 11(c), (g) enlarged images of region ii in Fig. 11 (d), and high-resolution images and selected electron diffraction patterns of region i in Fig. 11(d) are shown in (e) and (f), respectively, while high-resolution image and selected electron diffraction patterns of region ii in Fig. 11(d) are shown in (h) and (i); the FFT diagrams for the position of the blue rectangular box are shown in Fig. 11(j)-(l), followed by their corresponding IFFT diagrams presented in Fig. 11(m)-(o).

EDS area scanning was performed in regions I and II of Fig. 11(b) to further clarify the compositional variations in the surrounding regions of the discharge channel. The EDS area scan corresponding to Fig. 12(e) reveals a higher concentration of Ti and O around the discharge channel, while the Si content is lower. Fig. 12(j) shows the EDS line scan results obtained from regions surrounding the discharge channel to areas away from it (indicated by the blue arrows in Fig. 12(e)). Once again, these findings demonstrate that the amorphous region encompassing the discharge channel contains a greater proportion of TiO_2 than does the polycrystalline region situated further away. The EDS area scan images in Figs. 12(f-h) correspond to the image in Fig. 12(a). It is evident that the concentrations of Ti and O decrease towards the periphery of the discharge channel, while Si is uniformly distributed throughout. In Fig. 12(i), a line scan across the position in Fig. 12(a) reveals an increase in the Si content as it approaches the coating surface. These findings are consistent with the preceding SEM analysis of the distribution of elements in the MAO coating section.

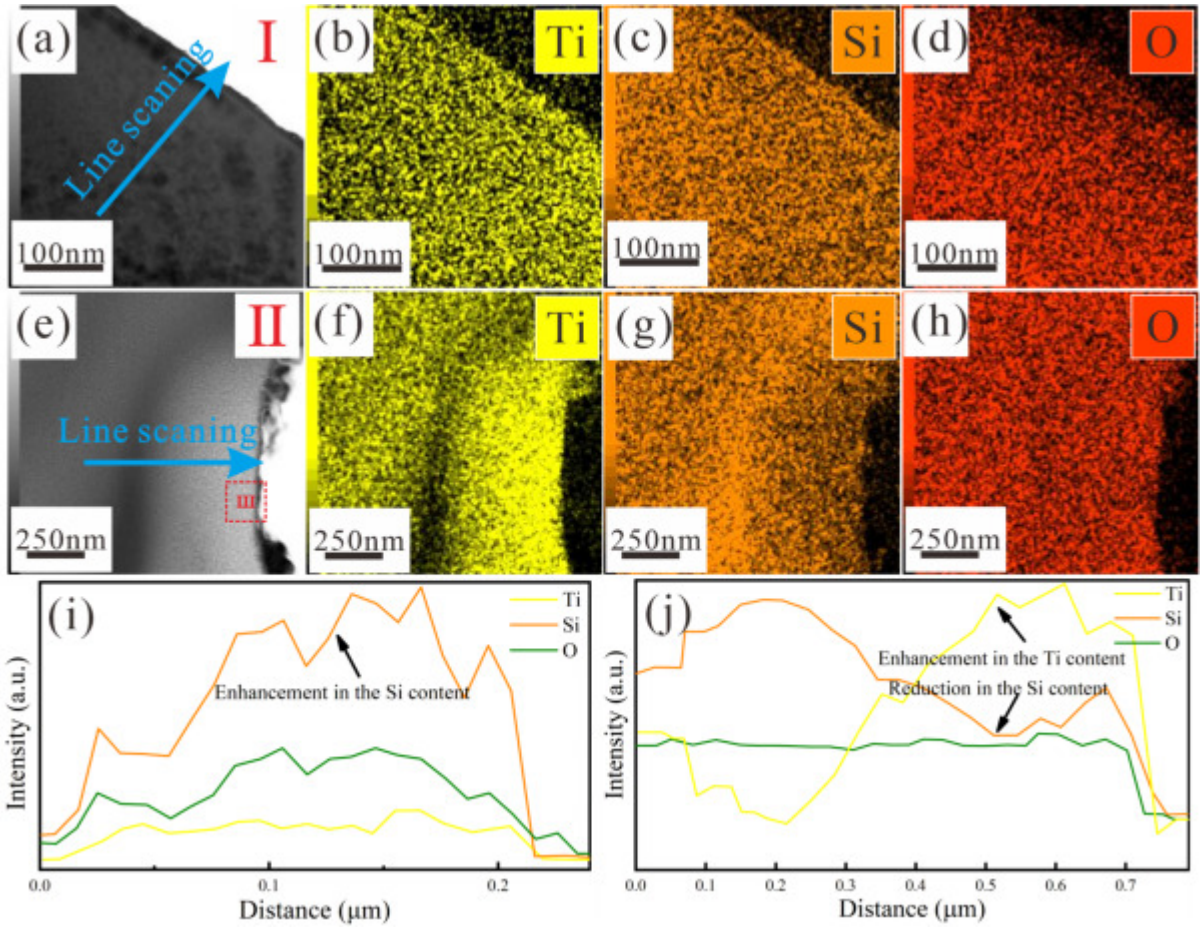

1. Download: Download high-res image (1MB)
2. Download: Download full-size image

Fig. 12. TEM bright field image, EDS line scan, and surface scan of the cross-sectional micropore in the MAO-0.15 coating are presented: (a)-(d) surface scan results of area I in Fig. 11(b); (e)-(h) surface scan results of area II in Fig. 11(b); (i) line scan image along the purple arrow in Fig. 12(a); and (j) line scan image along the purple arrow in Fig. 12(e).

4. Discussion

The MAO process that occurs on the surface of Ti6Al4V can be categorized into three consecutive stages. Fig. 13 illustrates the role of OH^- in each of those stages. In the initial stage, a thin anodized

layer is formed on the substrate through an electrochemical reaction and associated physical processes, while numerous small gas bubbles are generated on the surface. The growth of the anodic oxide layer at this stage is driven by the difference in electrode potential between Ti and O [49], with O primarily originating from the oxidation reactions of OH^- and O^{2-} [50].

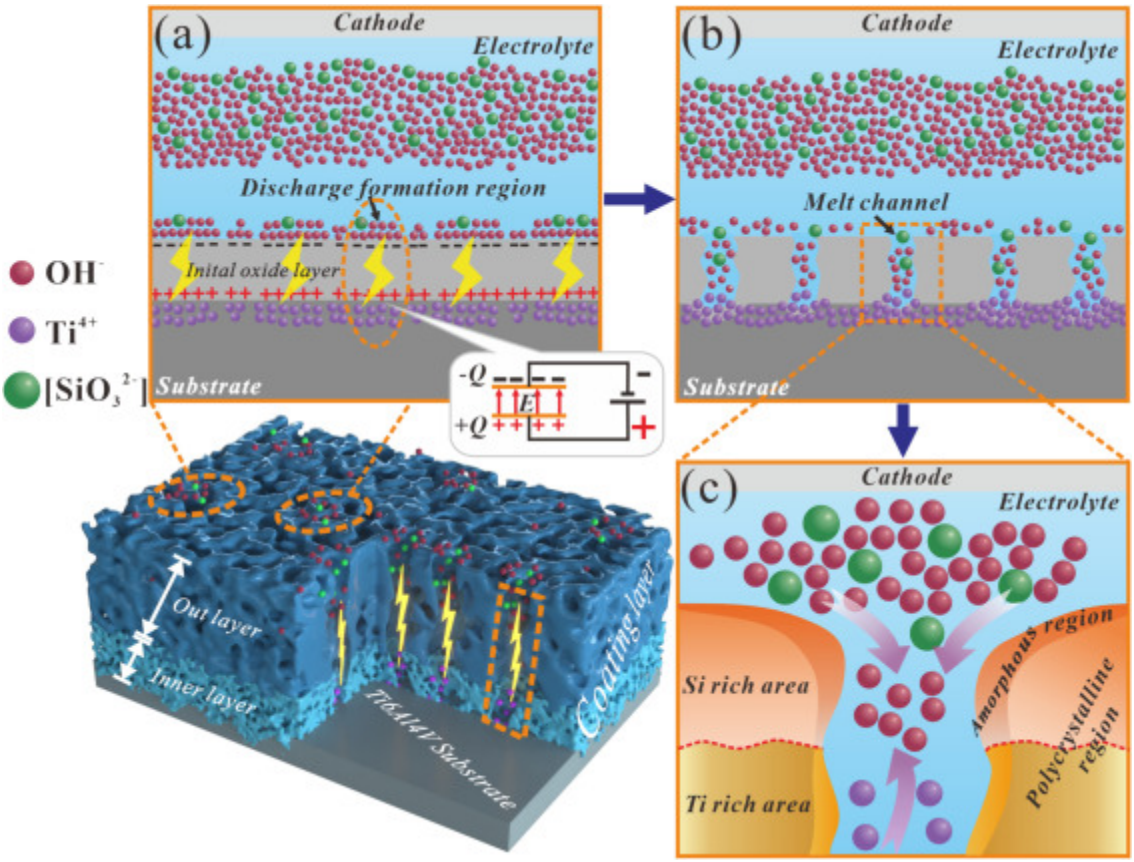

1. Download: Download high-res image (1MB)
2. Download: Download full-size image

Fig. 13. Diagram of the coating evolution of the Ti6Al4V alloy during MAO treatment. (a) When a voltage is applied, the anions in the electrolyte undergo adsorption onto the positively charged substrate, resulting in dielectric breakdown and discharge; (b) the discharge region forms a localized melt channel; (c) the growth mechanism of a single discharge channel.

The second stage of the MAO process is schematically illustrated in Fig. 13(a). When NaOH is introduced into the silicate electrolyte system, the relative migration rate of ions is influenced by their particle size and charge. Since OH^- has a higher migration rate than SiO_3^{2-} under an electric field, it reaches the surface of the anode more rapidly. The negative charge on the oxide layer surface increases with increasing OH^- concentration. Simultaneously, cationic charges such as Ti^{4+} accumulate at the interface between the oxide layer and the metal substrate. Therefore, on the surface of the original preformed oxide layer, positively and negatively charged aggregation pairs are formed at many local locations. At this juncture, the charge accumulated at both ends of the oxide layer is similar to that of a capacitor, and when the positive and negative charges continue to accumulate, the potential difference at both ends of the oxide layer will continue to increase. When it is sufficient to break down the oxide layer, it will cause a discharge phenomenon and eventually lead to simultaneous discharge at multiple points on the surface of the oxide layer. Discharge can occur anywhere within this layer depending on its strength, including at the interface between metal and

oxide or that between oxide and electrolyte [51,52]. Following breakdown, due to the high pressure and heat energy from discharge, a local melt channel forms in regions where preformed oxide layers exist [51], as depicted in Fig. 13(b). Components present in this melt zone from both the electrolyte and substrate can be ionized by a strong electric field induced by an applied voltage [53,54]. The resulting OH^-, SiO_3^{2-}, and Ti^{4+} plasmas generated within this region can be incorporated into coatings through the following plasma chemical reactions.(1)Ti4++4OH−→TiO2+2H2O(2)4OH−→O2↑+2H2O+4e−(3)SiO32−→SiO2+1/2O2+2e−(4)SiO32−l+H2Ol→PlasmaSiO2s+2OH−l

Different types of discharges occur during the MAO process, which Hussein et al. [52] classified into three categories: A, B, and C. The B-type discharge originates at the substrate-coating interface, establishing a channel from the substrate to the coating surface, thus forming interconnected pores throughout the coating. Such interconnected pores promote the diffusion of OH^- ions. This is conducive to the micropore formation process, and each discharge and spark can breakdown the oxide layer, forming a plasma discharge channel, thereby increasing the ion flow, electron flow and melting current of the oxide layer. In addition, due to the high intensity of B-type discharge and the large heat-affected zone (HAZ), including the adjacent coating and the bottom substrate, the transfer of OH^- to the Ti6Al4V substrate through the discharge channel is enhanced under the action of thermal diffusion, which can be verified by the presence of a large dome-like projection on the substrate, as shown in Fig. 9. As a result, more of the substrate is dissolved, allowing more Ti to participate in subsequent plasma reactions and form more titanium oxide phases.

Third, as the reaction progresses, the plasma bubbles expand. Under high-pressure conditions, a majority of the plasma is expelled from the discharge channel into the electrolyte, while a residual portion forms an inner layer at the interface between the substrate and coating. During this process, owing to the high-energy characteristics of the discharge channel, plasma exhibits a significant ability to dissolve substantial amounts of oxides at elevated temperatures and often transforms into amorphous and crystalline states upon cooling from the molten state [55], as previously confirmed by FIB-TEM analysis. Ultimately, a layered distribution is observed around the discharge channel structure, with amorphous components predominantly present in proximity to it, whereas distinct crystal structures are evident further away from it (Fig. 11). Additionally, the plasma that erupts outwards gradually cools through interactions with the cold electrolyte. Oxides with high freezing points, such as titanium oxide, undergo initial solidification (reactions (1)) and subsequently deposit on the channel wall. Conversely, liquid oxides with lower freezing points, such as silica, consistently solidify at the mouth of the channel (reactions (3)–(4)). Some inorganic ions, such as SiO_3^{2-}, dissolve in cold electrolytes. As a result, Ti is located more in the inner layer than in the outer layer. In the silicate electrolyte without the addition of NaOH, less substrate is dissolved, and more electrolyte is involved in the plasma reaction. With the addition of NaOH to the electrolyte, the dissolution of the substrate increases, and more Ti ions enter the discharge channel. Thus, as shown in Fig. 9, the titanium oxide content in the inner layer of the coating increases as the concentration of NaOH increases.

The discharge breakdown results in the formation of a slightly thicker coating, after which the new coating rebreaks the weak spot of the coating at a slightly higher potential difference in the next cycle, repeatedly undergoing melting, melt expansion, resolidification, diffusion, sintering, and condensation [52,[56], [57], [58]]. Finally, with the combined action of different discharge types, the MAO coating can continue to grow and rebuild over its entire thickness [59].

Recently, the antibacterial coating of medical grade Ti alloys has emerged as a prominent area of research. Although the incorporation of antibiotics into the surface coating of such alloys is widely practiced, achieving sustained drug release remains a challenge due to their short-term and rapid release characteristics [60,61]. By utilizing a porous loaded platform based on a MAO film in conjunction with a drug-releasing nanocontainer, it is possible to develop antibacterial coatings that enhance the biological properties of the titanium alloy implants, while reducing the infection risks. Therefore, incorporating NaOH in the electrolyte, for controlling the porous structure within the MAO layer offers a promising approach for achieving optimal drug loading capacity and sustained release.

5. Conclusion

In this work, MAO coatings on a Ti6Al4V alloy were synthesized through the addition of NaOH to a silicate electrolyte using a simple one-step MAO process. The addition of NaOH enables control over the pore size and density of the coating, so as to tune its biocompatibility. The proposed approach holds great potential for fabricating porous structures with exceptional drug-loading capacity, facilitating sustained drug release in bone implant applications, and mitigating the risk of implant failure. The following conclusions can be drawn on the basis of this work.

The energy release processes can be controlled by varying the NaOH concentration. As the concentration of NaOH increases, the breakdown voltage and energy consumption of the coated samples decrease. NaOH facilitates the generation of highly efficient discharges and sparks, effectively disrupting the oxide layer and establishing a plasma discharge channel. Microstructural analysis revealed that the surface porosity, pore size, and thickness of the MAO coatings increased with increasing NaOH concentration. The outer layer mainly contains SiO_2, while the inner layer is predominantly composed of titanium oxide. The structure surrounding the discharge channel exhibits distinct layered band characteristics. Near the discharge channel, an amorphous primary structure is observed, which gradually transitions into a recognizable crystal structure with increasing distance.

CRediT authorship contribution statement

Zongqing Liu: Writing – original draft, Methodology, Formal analysis, Data curation. **Wei Shi:** Writing – review & editing, Validation, Supervision, Resources, Project administration, Methodology, Conceptualization. **Song Xiang:** Visualization, Validation. **Fei Liu:** Writing – review & editing, Methodology. **Upadrasta Ramamurty:** Writing – review & editing, Resources.

Declaration of competing interest

The authors declare that they have no known competing financial interests or personal relationships that could have appeared to influence the work reported in this paper.

Acknowledgements

This work is supported by the China National Natural Science Foundation (Grant Nos. 52161010, 51974097 and 52301137), and the Guizhou Province Science and Technology Project (Grant No. 2022050). Major achievements transformation project in Guizhou Province (Grant No. 2023001). FL and UR acknowledge the support of their research by the Agency for Science, Technology and Research (A*STAR) of Singapore via the Structural Metal Alloys Programme (No. A18B1b0061) grant.

Data availability

Data will be made available on request.

References

1. [1]

M. Sarraf, E. Rezvani Ghomi, S. Alipour, S. Ramakrishna, N. Liana Sukiman

A state-of-the-art review of the fabrication and characteristics of titanium and its alloys for biomedical applications
Bio-Des. Manuf., 5 (2022), pp. 371-395
CrossrefView in ScopusGoogle Scholar

2. [2]

H. Attar, S. Ehtemam-Haghighi, N. Soro, D. Kent, M.S. Dargusch
Additive manufacturing of low-cost porous titanium-based composites for biomedical applications: advantages, challenges and opinion for future development
J. Alloys Compd., 827 (2020), Article 154263
View PDFView articleView in ScopusGoogle Scholar

3. [3]

G. Wu, Y. Yin, S. Zhang, Y. Wang, Y. Xiang, L. Li, J. Yao
Effect of laser texturing on the antiwear properties of microarc oxidation coating formed on Ti-6Al-4 V
Surf. Coat. Technol., 453 (2023), Article 129114
View PDFView articleView in ScopusGoogle Scholar

4. [4]

N. Jagadeeshanayaka, S. Awasthi, S.C. Jambagi, C. Srivastava
Bioactive surface modifications through thermally sprayed hydroxyapatite composite coatings: a review of selective reinforcements, biomaterials
Science, 10 (2022), pp. 2484-2523
CrossrefView in ScopusGoogle Scholar

5. [5]

H.C. Li, D.G. Wang, C. Hu, J.H. Dou, H.J. Yu, C.Z. Chen
Effect of Na(2)O and ZnO on the microstructure and properties of laser cladding derived CaO-SiO(2) ceramic coatings on titanium alloys
J. Colloid Interface Sci., 592 (2021), pp. 498-508
View PDFView articleView in ScopusGoogle Scholar

6. [6]

N. Singh, P. Hameed, R. Ummethala, G. Manivasagam, K.G. Prashanth, J. Eckert
Selective laser manufacturing of Ti-based alloys and composites: impact of process parameters, application trends, and future prospects
Materials Today, Advances, 8 (2020), Article 100097
View PDFView articleView in ScopusGoogle Scholar

7. [7]

R. Khanna, T. Kokubo, T. Matsushita, Y. Nomura, N. Nose, Y. Oomori, T. Yoshida, K. Wakita, H. Takadama
Novel artificial hip joint: a layer of alumina on Ti–6Al–4 V alloy formed by microarc oxidation
Mater. Sci. Eng. C, 55 (2015), pp. 393-400
View PDFView articleView in ScopusGoogle Scholar

8. [8]

J. Zhou, L. Zhao
Hypoxia-mimicking co doped TiO2 microporous coating on titanium with enhanced angiogenic and osteogenic activities
Acta Biomater., 43 (2016), pp. 358-368

View PDFView articleGoogle Scholar

9. [9]

G. Li, H. Cao, W. Zhang, X. Ding, G. Yang, Y. Qiao, X. Liu, X. Jiang

Enhanced Osseointegration of hierarchical Micro/Nanotopographic titanium fabricated by microarc oxidation and electrochemical treatment

ACS Appl. Mater. Interfaces, 8 (2016), pp. 3840-3852

CrossrefView in ScopusGoogle Scholar

10. [10]

P. Xiu, Z. Jia, J. Lv, C. Yin, Y. Cheng, K. Zhang, C. Song, H. Leng, Y. Zheng, H. Cai, Z. Liu

Tailored surface treatment of 3D printed porous Ti6Al4V by microarc oxidation for enhanced Osseointegration via optimized bone in-growth patterns and interlocked bone/implant Interface

ACS Appl. Mater. Interfaces, 8 (2016), pp. 17964-17975

CrossrefView in ScopusGoogle Scholar

11. [11]

S.-P. Kim, H.-R. Cho, H.-C. Choe

Bioactive element coatings on nanomesh formed Ti-6Al-4 V alloy surface using plasma electrolytic oxidation

Surf. Coat. Technol., 406 (2021), Article 126649

View PDFView articleView in ScopusGoogle Scholar

12. [12]

S. Arun, B.-S. Lim, S.-G. Ahn, H.-C. Choe

Osteoconductive element-doped, porous, and low-elastic-modulus duplex coatings on a Ti-6Al-4 V alloy: a hybrid coating system for accelerating cell growth

J. Alloys Compd., 943 (2023), Article 169131

View PDFView articleView in ScopusGoogle Scholar

13. [13]

A. Fukuda, M. Takemoto, T. Saito, S. Fujibayashi, M. Neo, D.K. Pattanayak, T. Matsushita, K. Sasaki, N . Nishida, T. Kokubo, T. Nakamura

Osteoinduction of porous Ti implants with a channel structure fabricated by selective laser melting

Acta Biomater., 7 (2011), pp. 2327-2336

View PDFView articleView in ScopusGoogle Scholar

14. [14]

T.Y. Kwak, J.Y. Yang, Y.B. Heo, S.J. Kim, S.Y. Kwon, W.J. Kim, D.H. Lim

Additive manufacturing of a porous titanium layer structure Ti on a co–Cr alloy for manufacturing cementless implants

J. Mater. Res. Technol., 10 (2021), pp. 250-267

View PDFView articleView in ScopusGoogle Scholar

15. [15]

W. Xu, Z. Liu, X. Lu, J. Tian, G. Chen, B. Liu, Z. Li, X. Qu, C. Wen

Porous Ti-10Mo alloy fabricated by powder metallurgy for promoting bone regeneration

Sci. China Mater., 62 (2019), pp. 1053-1064

CrossrefGoogle Scholar

16. [16]

W. Zhou, T. Wang, Y. Gan, J. Yang, H. Zhu, A. Wang, Y. Wang, W. Xi

Effect of micropore/microsphere topography and a silicon-incorporating modified titanium plate surface on the adhesion and osteogenic differentiation of BMSCs
Artificial Cells, Nanomedicine, and Biotechnology, 48 (2020), pp. 230-241
CrossrefView in ScopusGoogle Scholar

17. [17]
J. Cui, S. Zhang, M. Huang, X. Mu, J. Hei, V. Yau, H. He
Micronano porous structured tantalum-coated dental implants promote osteogenic activity in vitro and enhance osseointegration in vivo
J. Biomed. Mater. Res. A, 111 (2023), pp. 1358-1371
CrossrefView in ScopusGoogle Scholar

18. [18]
V. Karageorgiou, D. Kaplan
Porosity of 3D biomaterial scaffolds and osteogenesis
Biomaterials, 26 (2005), pp. 5474-5491
View PDFView articleView in ScopusGoogle Scholar

19. [19]
S. Kanwar, O. Al-Ketan, S. Vijayavenkataraman
A novel method to design biomimetic, 3D printable stochastic scaffolds with controlled porosity for bone tissue engineering
Mater. Des., 220 (2022), Article 110857
View PDFView articleView in ScopusGoogle Scholar

20. [20]
S.J. Lee, J.S. Choi, K.S. Park, G. Khang, Y.M. Lee, H.B. Lee
Response of MG63 osteoblast-like cells onto polycarbonate membrane surfaces with different micropore sizes
Biomaterials, 25 (2004), pp. 4699-4707
View PDFView articleView in ScopusGoogle Scholar

21. [21]
Y. Li, Y. Xiao, C. Liu
The horizon of Materiobiology: a perspective on material-guided cell behaviors and tissue engineering
Chem. Rev., 117 (2017), pp. 4376-4421
CrossrefView in ScopusGoogle Scholar

22. [22]
W. Zhou, O. Huang, Y. Gan, Q. Li, T. Zhou, W. Xi
Effect of titanium implants with coatings of different pore sizes on adhesion and osteogenic differentiation of BMSCs
Artificial Cells, Nanomedicine, and Biotechnology, 47 (2019), pp. 290-299
CrossrefView in ScopusGoogle Scholar

23. [23]
P.A.B. Kuroda, M.C. Rossi, C.R. Grandini, C.R.M. Afonso
Assessment of applied voltage on the structure, pore size, hardness, elastic modulus, and adhesion of anodic coatings in ca-, P-, and mg-rich produced by MAO in Ti–25Ta–Zr alloys
J. Mater. Res. Technol., 26 (2023), pp. 4656-4669
View PDFView articleView in ScopusGoogle Scholar

24. [24]
H. Li, G. Ma, Z. Wang
Corrosion behavior of ZrO2-TiO2 composite coatings produced on titanium alloy via plasma electrolytic oxidation
Surf. Coat. Technol., 469 (2023), Article 129814
View PDFView articleView in ScopusGoogle Scholar
25. [25]
Z. Guo, Z. Yang, Y. Chen, H. Li, Q. Zhao, Y. Xu, H. Zhan, J. Hao, Y. Zhao
One-step plasma electrolytic oxidation with graphene oxide for ultralow porosity corrosion-resistant TiO2 coatings
Appl. Surf. Sci., 594 (2022), Article 153477
View PDFView articleView in ScopusGoogle Scholar
26. [26]
L. Xie, X. Liao, G. Yin, Z. Huang, D. Yan, Y. Yao, W. Liu, X. Chen, J. Gu
Preparation, characterization, in vitro bioactivity, and osteoblast adhesion of multilevel porous titania layer on titanium by two-step anodization treatment
J. Biomed. Mater. Res. A, 98A (2011), pp. 312-320
View PDFView articleCrossrefGoogle Scholar
27. [27]
L. Xie, X. Liao, H. Xu, G. Yin, Z. Huang, Y. Yao, X. Chen, J. Gu
A facile one-step anodization treatment to prepare multilevel porous titania layer on titanium
Mater. Lett., 72 (2012), pp. 141-144
View PDFView articleView in ScopusGoogle Scholar
28. [28]
Z. Liu, W. Wang, H. Liu, T. Wang, M. Qi
Formation and characterization of titania coatings with cortex-like slots formed on Ti by microarc oxidation treatment
Appl. Surf. Sci., 266 (2013), pp. 250-255
View PDFView articleView in ScopusGoogle Scholar
29. [29]
D.S. Doolabi, M. Ehteshamzadeh, S.M.M. Mirhosseini
Effect of NaOH on the structure and corrosion performance of alumina and silica PEO coatings on aluminum
J. Mater. Eng. Perform., 21 (2012), pp. 2195-2202
CrossrefGoogle Scholar
30. [30]
Z.U. Rehman, C. Jeong, D.J. Choi
Effect of NaOH concentration on the microstructure and mechanical properties of the PEO coatings on mg-Al3-Zn1 alloy
Mater. Sci. Forum, 977 (2020), pp. 83-89
CrossrefView in ScopusGoogle Scholar
31. [31]
R. Zhou, D. Wei, W. Feng, S. Cheng, H. Yang, B. Li, Y. Wang, D. Jia, Y. Zhou
Bioactive coating with hierarchical double porous structure on titanium surface formed by two-step

microarc oxidation treatment
Surf. Coat. Technol., 252 (2014), pp. 148-156
View PDFView articleView in ScopusGoogle Scholar
32. [32]
S. Stojadinović, N. Radić, R. Vasilić, M. Petković, P. Stefanov, L. Zeković, B. Grbić
Photocatalytic properties of TiO2/WO3 coatings formed by plasma electrolytic oxidation of titanium in 12-tungstosilicic acid
Appl. Catal. Environ., 126 (2012), pp. 334-341
View PDFView articleView in ScopusGoogle Scholar
33. [33]
S. Guan, M. Qi, Y. Li, W. Wang
Morphology evolution of the porous coatings on Ti–xAl alloys by Al adding into Ti during microarc oxidation in Na2B4O7 electrolyte
Surf. Coat. Technol., 395 (2020), Article 125948
View PDFView articleView in ScopusGoogle Scholar
34. [34]
H. Sampatirao, S. Amruthaluru, P. Chennampalli, R.K. Lingamaneni, R. Nagumothu
Fabrication of ceramic coatings on the biodegradable ZM21 magnesium alloy by PEO coupled EPD followed by laser texturing process
Journal of Magnesium and Alloys, 9 (2021), pp. 910-926
View PDFView articleView in ScopusGoogle Scholar
35. [35]
S. Guan, M. Qi, C. Wang, S. Wang, W. Wang
Enhanced cytocompatibility of Ti6Al4V alloy through selective removal of Al and V from the hierarchical microarc oxidation coating
Appl. Surf. Sci., 541 (2021), Article 148547
View PDFView articleView in ScopusGoogle Scholar
36. [36]
F.C. Walsh, C.T.J. Low, R.J.K. Wood, K.T. Stevens, J. Archer, A.R. Poeton, A. Ryder
Plasma electrolytic oxidation (PEO) for production of anodized coatings on lightweight metal (Al, mg, Ti) alloys
Trans. IMF, 87 (2009), pp. 122-135
View in ScopusGoogle Scholar
37. [37]
I. Han, J.H. Choi, B.H. Zhao, H.K. Baik, I.-S. Lee
Microarc oxidation in various concentration of KOH and structural change by different cut off potential
Curr. Appl. Phys., 7 (2007), pp. e23-e27
View PDFView articleView in ScopusGoogle Scholar
38. [38]
E. Matykina, R. Arrabal, M. Mohedano, B. Mingo, J. Gonzalez, A. Pardo, M.C. Merino
Recent advances in energy efficient PEO processing of aluminium alloys
Trans. Nonferrous Met. Soc. Chin., 27 (2017), pp. 1439-1454
View PDFView articleView in ScopusGoogle Scholar
39. [39]

S. Stojadinović, R. Vasilić, M. Petković, B. Kasalica, I. Belča, A. Žekić, L. Zeković
Characterization of the plasma electrolytic oxidation of titanium in sodium metasilicate
Appl. Surf. Sci., 265 (2013), pp. 226-233
View PDFView articleView in ScopusGoogle Scholar

40. [40]
D.A.H. Hanaor, C.C. Sorrell
Review of the anatase to rutile phase transformation
J. Mater. Sci., 46 (2011), pp. 855-874
CrossrefView in ScopusGoogle Scholar

41. [41]
S. Aliasghari, P. Skeldon, G.E. Thompson
Plasma electrolytic oxidation of titanium in a phosphate/silicate electrolyte and tribological performance of the coatings
Appl. Surf. Sci., 316 (2014), pp. 463-476
View PDFView articleView in ScopusGoogle Scholar

42. [42]
M. Mu, X. Zhou, Q. Xiao, J. Liang, X. Huo
Preparation and tribological properties of self-lubricating TiO2/graphite composite coating on Ti6Al4V alloy
Appl. Surf. Sci., 258 (2012), pp. 8570-8576
View PDFView articleView in ScopusGoogle Scholar

43. [43]
X. Tao, Z. Yao, X. Luo
Comparison of tribological and corrosion behaviors of Cp Ti coated with the TiO2/graphite coating and nitrided TiO2/graphite coating
J. Alloys Compd., 718 (2017), pp. 126-133
View PDFView articleView in ScopusGoogle Scholar

44. [44]
F. Wang, L. Feng, Y. Qin, T. Zhao, H. Luo, J. Zhu
Dual functional SiO2@TiO2 photonic crystals for dazzling structural colors and enhanced photocatalytic activity
J. Mater. Chem. C, 7 (2019), pp. 11972-11983
CrossrefView in ScopusGoogle Scholar

45. [45]
N. Ao, D. Liu, S. Wang, Q. Zhao, X. Zhang, M. Zhang
Microstructure and Tribological behavior of a TiO2/hBN composite ceramic coating formed via microarc oxidation of Ti–6Al–4 V alloy
Journal of Materials Science & Technology, 32 (2016), pp. 1071-1076
View PDFView articleView in ScopusGoogle Scholar

46. [46]
Q. Li, W. Yang, C. Liu, D. Wang, J. Liang
Correlations between the growth mechanism and properties of microarc oxidation coatings on titanium alloy: effects of electrolytes
Surf. Coat. Technol., 316 (2017), pp. 162-170

View PDFView articleGoogle Scholar
47. [47]
T.H. Teh, A. Berkani, S. Mato, P. Skeldon, G.E. Thompson, H. Habazaki, K. Shimizu
Initial stages of plasma electrolytic oxidation of titanium
Corros. Sci., 45 (2003), pp. 2757-2768
View PDFView articleView in ScopusGoogle Scholar
48. [48]
M. Shokouhfar, S.R. Allahkaram
Formation mechanism and surface characterization of ceramic composite coatings on pure titanium prepared by microarc oxidation in electrolytes containing nanoparticles
Surf. Coat. Technol., 291 (2016), pp. 396-405
View PDFView articleView in ScopusGoogle Scholar
49. [49]
X. Wang, B. Li, L. Zhou, J. Ma, X. Zhang, H. Li, C. Liang, S. Liu, H. Wang
Influence of surface structures on biocompatibility of TiO2/HA coatings prepared by MAO
Mater. Chem. Phys., 215 (2018), pp. 339-345
View PDFView articleGoogle Scholar
50. [50]
Y. Gong, J. Geng, J. Huang, Z. Chen, M. Wang, D. Chen, H. Wang
Self-healing performance and corrosion resistance of novel CeO2-sealed MAO film on aluminum alloy
Surf. Coat. Technol., 417 (2021), Article 127208
View PDFView articleView in ScopusGoogle Scholar
51. [51]
R.O. Hussein, X. Nie, D.O. Northwood, A. Yerokhin, A. Matthews
Spectroscopic study of electrolytic plasma and discharging behaviour during the plasma electrolytic oxidation (PEO) process
J. Phys. D Appl. Phys., 43 (2010), Article 105203
CrossrefView in ScopusGoogle Scholar
52. [52]
R.O. Hussein, X. Nie, D.O. Northwood
An investigation of ceramic coating growth mechanisms in plasma electrolytic oxidation (PEO) processing
Electrochim. Acta, 112 (2013), pp. 111-119
View PDFView articleView in ScopusGoogle Scholar
53. [53]
X. Lu, C. Blawert, K.U. Kainer, M.L. Zheludkevich
Investigation of the formation mechanisms of plasma electrolytic oxidation coatings on mg alloy AM50 using particles
Electrochim. Acta, 196 (2016), pp. 680-691
View PDFView articleView in ScopusGoogle Scholar
54. [54]
G. Rapheal, S. Kumar, N. Scharnagl, C. Blawert
Effect of current density on the microstructure and corrosion properties of plasma electrolytic

oxidation (PEO) coatings on AM50 mg alloy produced in an electrolyte containing clay additives
Surf. Coat. Technol., 289 (2016), pp. 150-164
View PDFView articleView in ScopusGoogle Scholar
55. [55]
V. Dehnavi, W.J. Binns, J.J. Noël, D.W. Shoesmith, B.L. Luan
Growth behaviour of low-energy plasma electrolytic oxidation coatings on a magnesium alloy
Journal of Magnesium and Alloys, 6 (2018), pp. 229-237
View PDFView articleView in ScopusGoogle Scholar
56. [56]
T.W. Clyne, S.C. Troughton
A review of recent work on discharge characteristics during plasma electrolytic oxidation of various metals
Int. Mater. Rev., 64 (2019), pp. 127-162
CrossrefView in ScopusGoogle Scholar
57. [57]
Y.-l. Cheng, Z.-g. Xue, Q. Wang, X.-Q. Wu, E. Matykina, P. Skeldon, G.E. Thompson
New findings on properties of plasma electrolytic oxidation coatings from study of an Al–cu–Li alloy
Electrochim. Acta, 107 (2013), pp. 358-378
View PDFView articleView in ScopusGoogle Scholar
58. [58]
M. Kaseem, S. Fatimah, N. Nashrah, Y.G. Ko
Recent progress in surface modification of metals coated by plasma electrolytic oxidation: principle, structure, and performance
Prog. Mater. Sci., 117 (2021), Article 100735
View PDFView articleView in ScopusGoogle Scholar
59. [59]
W.-w. Chen, Z.-x. Wang, L. Sun, S. Lu
Research of growth mechanism of ceramic coatings fabricated by microarc oxidation on magnesium alloys at high current mode
Journal of Magnesium and Alloys, 3 (2015), pp. 253-257
View PDFView articleView in ScopusGoogle Scholar
60. [60]
R. He, J. Sui, G. Wang, Y. Wang, K. Xu, S. Qin, S. Xu, F. Ji, H. Zhang
Polydopamine and hyaluronic acid immobilization on vancomycin-loaded titanium nanotube for prophylaxis of implant infections
Colloids Surf. B Biointerfaces, 216 (2022), Article 112582
View PDFView articleView in ScopusGoogle Scholar
61. [61]
S. Xiao, L. Yuan, J. Liu, G. Li, Q. Zou, Y. Zuo, J. Li, Y. Li
Vancomycin-loaded silica coatings for controlled release of drug and Si ions to repair infected bone defects
Surf. Coat. Technol., 463 (2023), Article 129525
View PDFView articleView in ScopusGoogle Scholar